Mon. Not. R. Astron. Soc. **000**, 000–000 (0000) Printed 11 October 2007 (MN LATEX style file v2.2)

Predicting the Properties of the Remnants of Dissipative Galaxy Mergers

M. Covington[1,4⋆†], A. Dekel[1,2], T. J. Cox[3], P. Jonsson[4], and J. R. Primack[1,4]
[1] *Department of Physics, University of California, 1156 High St., Santa Cruz, 95064, USA*
[2] *Racah Institute of Physics, The Hebrew University, Jerusalem, 91904, Israel*
[3] *Harvard-Smithsonian Center for Astrophysics, 60 Garden St., Cambridge, MA 02138, USA*
[4] *Santa Cruz Institute of Particle Physics, University of California, 1156 High St., Santa Cruz, 95064, USA*

11 October 2007

ABSTRACT
We construct a physically motivated model for predicting the properties of the remnants of gaseous galaxy mergers, given the properties of the progenitors and the orbit. The model is calibrated using a large suite of SPH merger simulations. It implements generalized energy conservation while accounting for dissipative energy losses and star formation. The dissipative effects are evaluated from the initial gas fractions and from the orbital parameters via an "impulse" parameter, which characterizes the strength of the encounter. Given the progenitor properties, the model predicts the remnant stellar mass, half-mass radius, and velocity dispersion to an accuracy of 25%. The model is valid for both major and minor mergers. We provide an explicit recipe for semi-analytic models of galaxy formation.

Key words: galaxies: interactions – galaxies: evolution – galaxies: elliptical and lenticular, cD – galaxies: formation – methods: .

1 INTRODUCTION

Major mergers between galaxies are central to the formation and evolution of elliptical galaxies (Toomre & Toomre 1972; Toomre 1977; Mihos & Hernquist 1994). The hierarchical buildup of galaxies in the ΛCDM cosmology consists of a sequence of mergers, of which a significant fraction are "major," involving progenitors with a mass ratio larger than 1:3. The gravitational interactions in such mergers have a dramatic effect on the dynamics and morphology of the galaxies, in particular turning rotating disks into pressure-supported spheroids. If the progenitors also contain gas, the mergers induce starbursts followed by gas consumption, which leads to aging stellar populations. The modeling of major mergers is therefore a key element in the attempts to confront the broad picture of galaxy formation with detailed observations. This is commonly performed via simulations incorporating Semi-Analytic Models (SAMs), where the complex physical processes are modeled using simplified parametric recipes.

Advanced SAMs are currently attempting the non-trivial task of following the sizes and internal velocities of galaxies. For disk galaxies, sizes are evaluated using the halo virial radii $R_{\rm vir}$ and spin parameters λ via $R_{\rm disk} \simeq \lambda R_{\rm vir}$, with some modifications due to the halo density profile (Fall & Efstathiou 1980; Mo, Mao & White; Bullock, Dekel et al. 2001; Dutton et al. 2006). The sizes of the remnants of gas-poor ("dry") mergers, where the dominant interaction is gravitational, can be extracted from the properties of the progenitors and the orbital energy by assuming conservation of energy and relaxation to virial equilibrium (Cole et al. 2000). These considerations work well in simulations of relatively dry mergers, quite independently of the details of the orbit.

While dry mergers may dominate in the formation of the most massive galaxies (Naab et al. 2006), the most common mergers are "wet" mergers of gaseous galaxies. It is thought that gas processes play an important role in the formation of ellipticals (Robertson et al. 2006; Dekel & Cox 2006; Ciotti et al. 2007). As demonstrated below, the sizes predicted by dissipationless energy conservation can be off by a factor of a few for gas-rich mergers. Our goal is to construct a more accurate recipe to predict the size and velocity dispersion of the remnant of a wet merger given the properties of the progenitors and the orbital parameters. Cosmological mergers involve a complex mixture of variables (such as orbital parameters, gas fractions, mass ratio and bulge fraction) and physical processes (such as star formation and feedback), all of which can influence the properties

⋆ National Science Foundation Graduate Fellow
† email: mdcovin@physics.ucsc.edu

of the merger remnants. Given a rich suite of high-resolution SPH merger simulations (Cox 2004; Cox et al. 2006), that span the available parameter space and physical processes, albeit in a rather sparse and nonuniform manner, we seek a model that will properly represent the simulation results and enable an interpolation between them as well as an extrapolation to outside the simulated regime.

For such a recipe to be successful, it should be based on a toy model that grasps the essence of the main physical processes involved in wet mergers. Our intuition is guided by the finding from the simulations that the remnants are more compact when the initial gas fraction is higher and when the first passage involves a stronger tidal impulse, namely when a larger fraction of the orbital energy turns into internal kinetic energy. At a first glance, this may seem surprising, as a system that gains energy is not expected to become more tightly bound, and indeed, the remnants of dry mergers are not very sensitive to the strength of the impulse. This dependence on gas fraction and on the impulse implies that a higher gas fraction and a stronger impulse are associated with a higher degree of dissipation, via shocks, collisions of gas clouds, and induced gas flows toward the centres of the merging systems. The resultant higher gas densities enhance the energy losses to radiation, leaving behind a more tightly bound remnant. In parallel, the higher degree of dissipation yields a stronger burst of star formation, which tends to be focused in the central region of the remnant. This understanding is the basis for our proposed recipe, which characterizes the merger by the impulse at first passage, evaluates the associated degree of dissipation and the resultant radiative energy losses and star formation, and accounts for these energy losses in the energy balance. A few free parameters with values of order unity can hopefully compensate for the crude approximations made. These approximations include, for example, an assumption of structural homology between the progenitors and remnant. The physically motivated recipe is then calibrated using the merger simulations, and its success is to be judged by its accuracy in matching the simulated remnant properties.

In §2 we describe the simulations used for this study. In §3 we present the details of our model for predicting remnant properties. In §4 we generalize the model to unequal mass mergers. In §5 we discuss certain limitations of our model, and in §6 we summarize our conclusions. Appendix A discusses the details of our impulse approximation. Appendix B presents an explicit recipe for SAMs.

2 MERGER SIMULATIONS

2.1 Numerical Code

The numerical simulations analyzed in this work are part of a large suite of galaxy merger simulations designed to study the induced star formation (Cox 2004; Cox et al. 2006) and observable counterparts (Jonsson 2006; Jonsson et al. 2006) of such events. Details of these simulations can be found in the above references, but we include here a brief description for completeness.

All numerical simulations performed in this work use the N-Body/SPH code GADGET (Springel, Yoshida & White 2001). Hydrodynamics are included via the Lagrangian technique of smoothed particle hydrodynamics (SPH). We use the "conservative entropy" version of SPH (Springel & Hernquist 2002). Gas is assumed, for simplicity, to be a primordial plasma that can radiatively cool via atomic and free-free emission.

All of the numerical simulations presented here include star formation. Stars are formed in regions of gas which are above a critical density for star formation at a rate proportional to the local gas density and inversely proportional to the local dynamical time-scale. The efficiency of star formation is fixed by requiring star formation to follow the observed correlation between gas and star-formation rate surface densities (Kennicutt 1998).

We also include a simple prescription to simulate the effects of feedback from massive stars. This feedback acts to pressurize the interstellar medium and regulates the conversion of gas to stars. Details of this model and the parameter choices can be found in Cox et al. (2006). Specifically, most simulations studied in this paper used the *n2med* parameter set. Under these assumptions the gas pressure increases as the density squared; i.e, star-forming gas has a "stiff" equation of state. Other cases are discussed in §5.

The simulations presented here adopt a gravitational softening length $h = 400$ pc for the dark matter particles and 100 pc for the stellar and gas particles. We remind the reader that, in GADGET, forces between neighboring particles become non-Newtonian for separations $< 2.3\,h$.

2.2 Initial Galaxies

All of the simulations presented here are mergers between two identical disk galaxies, except for cases discussed in §4. The disk galaxy models are motivated by observations of low-redshift galaxies. In some cases we made systematic studies of varying progenitor galaxy properties (e.g. varying gas fraction in the G3 gas fraction series). While many of these varied cases would not look like typical low-redshift galaxies, we made no attempt to systematically vary properties in such a way as to capture variation with redshift. Furthermore, the simulations are not cosmological since the two galaxies are isolated. Disk galaxies are constructed in equilibrium and contain dark matter, an exponential stellar disk, an extended exponential gas disk, and some contain a dense central bulge. Our suite consists of five main types of models, detailed in Table 1:

(i) Z galaxies are gas-poor bulgeless disks and are roughly modeled after the Milky Way.
(ii) D galaxies are $\frac{1}{100}$ of the mass of the Z's, are bulgeless disks, and have a high gas fraction.
(iii) Y galaxies are $\frac{1}{10}$ of the mass of the Z's, are bulgeless disks, and have a high gas fraction.
(iv) Sbc galaxies are modeled after local Sbc-type spirals, with a small bulge and high gas fraction.
(v) G galaxies span a range of mass, bulge fraction, and gas fraction. Their properties are taken from statistical samples of local galaxies, including the SDSS. Their dark matter halos have not been adiabatically contracted (Blumenthal et al. 1984; Mo et al. 1998), unlike all the other models.

The ratio of the gas to stellar exponential radii varies with model type. For the Z, D, and Y models, the gas and stellar radii are equal. For the Sbc and G models, the gas

Table 1. Properties of progenitor galaxy models. $M_{\rm tot}$ is total mass, baryons plus dark matter; c is concentration ($R_{\rm vir}/r_{\rm s}$); $M_{\rm stars}$ is the initial stellar mass; B/D is the bulge-to-disk ratio; $f_{\rm g}$ is the initial gas mass divided by $M_{\rm tot}$; $R_{1/2}$ is the initial three-dimensional stellar half mass radius.

Type	$M_{\rm tot}$ ($10^{10}{\rm M}_\odot$)	c	$M_{\rm stars}$ ($10^{10}{\rm M}_\odot$)	B/D	$f_{\rm g}$	$R_{1/2}$ (kpc)
Milky Way Series						
D	1.4	20	0.036	0	0.025	1.16
Y	14.0	15	0.3	0	0.02	2.85
Z	143.0	12	5.1	0	0.004	4.04
Sbc Series						
Sbc	81.4	11	4.92	0.26	0.066	7.15
G Series						
G0	5.0	14	0.1	0.02	0.012	1.84
G1	20.0	12	0.5	0.06	0.010	2.33
G2	51.0	9	1.5	0.11	0.009	2.90
G3	116.0	6	5.0	0.22	0.011	3.90
G3 Gas Fraction Series						
G3gf1	116.0	6	3.6	0.32	0.023	3.49
G3gf2	116.0	6	2.6	0.52	0.031	2.89
G3gf3	116.0	6	1.5	1.34	0.040	1.77
G3gf4	116.0	6	5.3	0.20	0.005	3.96

radii are three times the stellar radii. For more detail on these models see Cox (2004).

2.3 Merger Orbits

The sizes of merger remnants are affected by the initial orbits and orientations. To understand this relationship a sufficient exploration of the merger orbit and orientation parameter space is required. To this end, we perform mergers on an identical orbit with various orientations of the merging galaxies (e.g. prograde and retrograde). We also perform mergers with many different orbits. Of all of the galaxy models, the Sbc models have the largest variety of orbits and orientations. The majority of the orbits in the suite are parabolic or near parabolic with eccentricities of 0.9 to 1.0. While these orbits are generally motivated by statistics from N-body simulations (Benson 2005; Khochfar & Burkert 2006), the distribution of orbits in the merger suite was not designed to exactly duplicate these statistics. Orbital parameters are given in Table 2.

3 MODELING PROPERTIES OF THE REMNANTS

3.1 Non-dissipative Energy Conservation Model

Energy conservation during the merger may be a useful constraint to impose. If the progenitors and the remnant are homologous, then energy conservation and the virial theorem may be applied to the stellar systems as if they are self-gravitating without introducing a large error. Current SAMs employ such considerations to predict merger remnant radii (Cole et al. 2000; Hatton et al. 2003). We start by summarizing the model of Cole et al.

In order to take orbital energy into account, this model assumes that the baryonic components of the progenitors spiral in under dynamical friction, losing energy to the outer dark matter halo, until reaching a distance that equals the sum of their three-dimensional stellar half-mass radii. Energy conservation is assumed from this point on. Thus the orbital energy term in the conservation equation is equal to the energy of a zero eccentricity (circular) orbit of the two galaxies with a constant separation equal to the sum of their half-mass radii,

$$\frac{(M_1+M_2)^2}{R_{\rm f}} = \frac{M_1^2}{R_1} + \frac{M_2^2}{R_2} + \frac{1}{c}\frac{M_1 M_2}{R_1+R_2}. \quad (1)$$

This equation relates the stellar three-dimensional half-mass radius of the remnant, $R_{\rm f}$, to the masses and three-dimensional stellar half-mass radii of the progenitors, M_1, M_2, R_1 and R_2, respectively. For major mergers, the masses are assumed to include the total stellar mass plus, as a rather arbitrary choice, twice the dark matter masses within R_1 and R_2 respectively. The constant c is a structural parameter which relates GM^2/R to the actual internal binding energy. It is assumed to take the same value, $c = 0.5$, for both the progenitors and the remnant.

This model, though crude, provides a general framework for estimating the outcome of a given merger. However, it has not been previously tested against realistic simulations that include gas dynamics and star formation. We begin by applying this recipe to the cases in our merger simulation suite. The predictions of the model are plotted against the actual half-mass radii of the simulated remnants in Figure 1. Throughout this paper we use the fractional rms scatter, S, to assess goodness of fit.

$$S = \sqrt{\frac{1}{N}\sum \frac{(P_{\rm predicted} - P_{\rm true})^2}{P_{\rm true}^2}}, \quad (2)$$

where P is some property that we are trying to predict from the initial conditions and are measuring from the simulation for comparison.

The predictions of this simple model deviate from the true radii by $S = 0.50$. Figure 1 shows that the model systematically over-predicts the radii of the remnants. This is a straightforward result of ignoring the radiative energy losses. Note that the predictions are best for the cases where the progenitors have the lowest gas fraction, cases Z and G3. For each type of progenitor, we see a wide spread in actual sizes for a given predicted size. This results from the variations in orbits and orientations, which are not addressed by the model. Despite the shortcomings of the dissipationless energy conservation model, it is a useful starting point. Our next goal is to correct for the dissipative effects.

3.2 A Toy Model for Radiative Losses

While the above dissipationless model works quite well in the case of low gas fraction, dissipative losses are likely to play an important role in the gas-rich mergers that were especially frequent in the early epochs of galaxy formation. In particular, they seem to be a crucial element in the forma-

Table 2. The orbital parameters of each of the simulations used in this study. Values are calculated from the orbital initial conditions assuming a point mass orbit. R_{peri} denotes pericentric distance. e denotes eccentricity. For equal mass mergers θ_1 and θ_2 denote the orientation of the first and second galaxy with respect to the orbital plane, where for $\theta_1 = 0$ the first galaxy is aligned with the orbital plane. For unequal mass mergers θ denotes the orientation of the orbit of the smaller progenitor with respect to the orientation of the larger progenitor. Again, $\theta = 0$ represents a case where the merger orbit aligns with the larger progenitor.

Major Mergers (55 runs)

name	R_{peri} (kpc)	e	θ_1	θ_2	name	R_{peri} (kpc)	e	θ_1	θ_2
D1mf-u1	1.1	1.0	0	30	Sbc201-u4	11.0	1.0	0	30
D2mf-u1	2.4	1.0	0	30	Sbc202-u4	11.0	1.0	180	30
D3mf-u1	4.1	1.0	0	30	Sbc203-u4	11.0	1.0	180	210
D4mf-u1	6.4	1.0	0	30	Sbc204-u4	5.5	1.0	0	30
D5mf-u1	8.9	1.0	0	30	Sbc205-u4	44.0	1.0	0	30
D6mf-u1	12.9	1.0	0	30	Sbc206-u4	11.0	1.0	90	30
D7mf-u1	0.6	1.0	0	30	Sbc207-u4	11.0	1.0	270	30
G0G0a-u1	2.24	0.95	-30	30	Sbc208-u4	5.5	1.0	180	30
G0G0r-u1	2.24	0.95	150	30	Sbc209-u4	5.5	1.0	180	210
G0G0-u1	2.24	1.0	-30	30	Sbc211-u4	44.0	1.0	180	210
G1G1a-u1	2.96	0.95	-30	30	Sbc212-u4	11.0	0.9	0	30
G1G1r-u1	2.96	0.95	150	30	Sbc213-u4	25.0	0.8	0	30
G2G2r-u1	3.82	0.95	150	30	Sbc214-u4	44.0	0.8	0	30
G2G2-u1	3.82	0.95	-30	30	Sbc215-u4	100.0	1.0	0	30
G3blv5G3blv5-u1	13.6	0.95	-30	30	Sbc216-u4	100.0	0.8	0	30
G3G3a-u1	13.6	0.95	-30	30	Sbc217-u4	11.0	1.0	90	90
G3G3b-u1	13.6	0.95	-30	30	Sbc218-u4	11.0	0.9	180	210
G3G3r-u1	13.6	0.95	150	30	Z2m-u1	7.1	1.0	0	30
G3gf1G3gf1b-u1	13.6	0.95	-30	30	Z7m-u1	21.4	0.9	0	30
G3gf2G3gf2b-u1	13.6	0.95	-30	30	Z8m-u1	35.7	0.8	0	30
G3gf3G3gf3b-u1	13.6	0.95	-30	30	Z9m-u1	1.7	1.0	0	30
G3gf4G3gf4b-u1	13.6	0.95	-30	30	Z10m-u1	3.9	1.0	0	30
Y1mf-u1	2.9	1.0	0	30	Z11m-u1	14.2	1.0	0	30
Y2mf-u1	5.7	1.0	0	30	Z12m-u1	22.2	1.0	0	30
Y3mf-u1	10.0	1.0	0	30	Z13m-u1	30.4	1.0	0	30
Y4mf-u1	15.7	1.0	0	30	Z14m-u1	44.7	1.0	0	30
Y5mf-u1	21.4	1.0	0	30	Z15m-u1	8.1	1.0	0	30
Y6mf-u1	31.4	1.0	0	30					

Minor Mergers (22 runs)

name	R_{peri} (kpc)	e	θ	Mass Ratio	name	R_{peri} (kpc)	e	θ	Mass Ratio
G1G0-u3	2.96	0.95	-30	1:3.9	G3G1f-u1	27.2	0.95	-30	1:5.8
G1G0r-u3	2.96	0.95	150	1:3.9	G3G1g-u1	64.4	0.95	-30	1:5.8
G2G0-u3	3.82	0.95	-30	1:10	G3G1h-u1	120	0	-30	1:5.8
G2G0r-u3	3.82	0.95	150	1:10	G3G2a-u1	13.6	0.95	0	1:2.3
G2G1-u3	3.82	0.95	-30	1:2.6	G3G2b-u1	13.6	0.95	-90	1:2.3
G2G1r-u3	3.82	0.95	150	1:2.6	G3G2c-u1	13.6	0.95	-60	1:2.3
G3G1a-u1	13.6	0.95	0	1:5.8	G3G2d-u1	13.6	0.95	180	1:2.3
G3G1b-u1	13.6	0.95	-90	1:5.8	G3G2e-u1	6.8	0.95	-30	1:2.3
G3G1c-u1	13.6	0.95	-60	1:5.8	G3G2f-u1	27.2	0.95	-30	1:2.3
G3G1d-u1	13.6	0.95	180	1:5.8	G3G2g-u1	64.4	0.95	-30	1:2.3
G3G1e-u1	6.8	0.95	-30	1:5.8	G3G2h-u1	120	0	-30	1:2.3

tion of the Fundamental Plane of elliptical galaxies (Robertson et al. 2006; Dekel & Cox 2006). We therefore wish to incorporate the radiative losses in our model.

When two gas-rich galaxies merge, a number of processes cause gas interactions and result in radiative energy losses. Tidal torques during a close pass can decrease the angular momentum in the gas disks and induce inflows into the galaxy centres. In a nearly radial encounter, the gas disk of one galaxy collides with that of the other creating shocks, which can result in loss of angular momentum. Furthermore, tidal forces during a merger introduce orbital crossings and density perturbations within the gas disks which ultimately lead to an increased gas collision rate. As the gas clouds collide and radiate away their kinetic energies, they fall toward the centre of the galactic potential well. This results in higher gas densities which lead to star formation and further radiative losses. Hence, the orbit, energy losses, and star formation are intimately linked.

The first step toward predicting energy losses from a given initial configuration is to characterize the perturbative

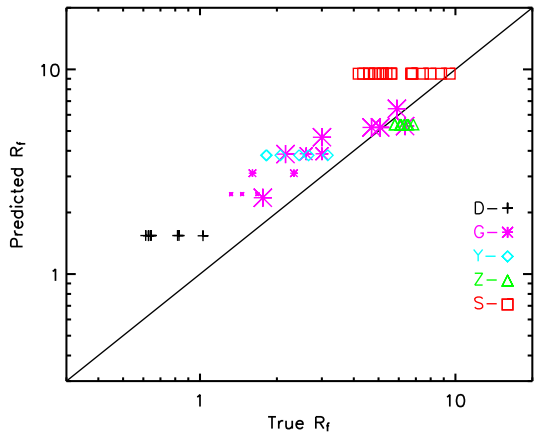

Figure 1. Dissipationless energy conservation model. The three-dimensional half-mass radii predicted by the model versus the actual radii in the simulated remnants. The symbols and colors denote the type of progenitors (Table 1): D (black crosses), G (purple asterisks), Y (blue diamonds), Z (green triangles) and Sbc (red squares). The symbols for G's have four different sizes which represent the different types of G progenitors. Larger symbols represent more massive galaxies. With a relatively large scatter of $S = 0.5$, this dissipationless model systematically over-predicts the sizes of the remnants, because it does not address the radiative energy losses.

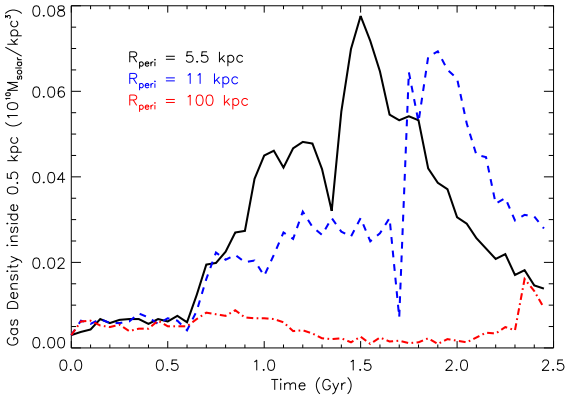

Figure 2. The central gas density in the inner 0.5 kpc during three separate Sbc mergers with initial orbital pericentric distances of 5.5, 11 and 100 kpc (solid black, dashed blue, and dash-dot red respectively). In all cases, the initial pass occurs at 0.6 Gyr. Final coalescences occur at roughly 1.5, 1.8 and 2.4 Gyr respectively. The plot demonstrates that the central gas density in the period following the first pass is increasing with decreasing pericentre distance, and that the density at the final coalescence is following the same trend.

strength of a given encounter. More specifically, we need to assess the dependence of the gas collisions and dissipation on the properties of the orbit. We find that the dissipation resulting from a given orbit can be characterized using the orbital parameters at the first close pass. This may seem surprising at first, since often most of the stars are formed in the final coalescence rather than at the initial encounter, but it can be explained by the sequence of events following the first pass. The gas disks are perturbed during the first pass, inducing a continuous gas in-fall toward the galactic centre, lasting ~ 1 Gyr. A stronger disturbance in the first pass leads to a larger buildup of gas in the progenitor centres. Some of this gas is involved in a first starburst immediately following the first pass, but a large fraction of this gas serves as a reservoir for star formation during the later stages of the merger, especially the violent final coalescence. Consequently, an orbit that is more disruptive on the first pass also suffers more energy losses, and forms more stars, during the final coalescence. This is illustrated in Figure 2.

During a close pass of two galaxies, orbital energy is injected into the internal kinetic energies of both galaxies. We define this "impulse" as the difference between the peak in the total internal kinetic energies during the encounter and the total initial internal kinetic energies of the two progenitors. We approximate the impulse on galaxy 1 by

$$\Delta E = \frac{AG^2 M_{1,\rm tot}^2 M_{2,\rm tot}}{V_{\rm peri}^2 (R_{\rm peri}^2 + B\ R_{1,\rm tot}\ R_{\rm peri} + C\ R_{1,\rm tot}^2)}, \qquad (3)$$

where $M_{1,\rm tot}$ and $M_{2,\rm tot}$ are the total mass of the perturbed and perturbing galaxies respectively, baryons plus dark matter, and $R_{1,\rm tot}$ is the total half mass radius of the perturbed galaxy. $R_{\rm peri}$ is the "pericentric distance" of the first passage, as calculated from the initial orbit assuming point masses.

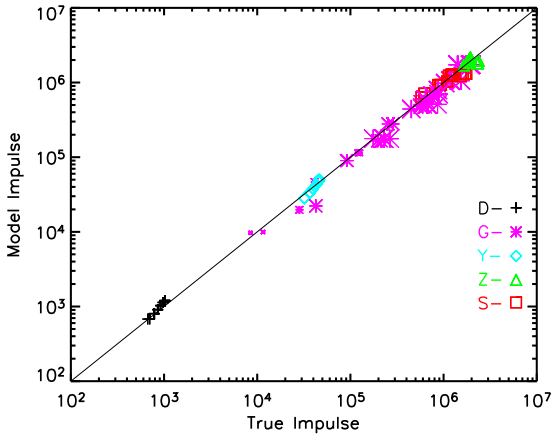

Figure 3. The approximation for the impulse against the measured impulse from the simulations. $S = 0.40$.

The best-fitting values of the parameters are found to be $A = 1.6$, $B = 1.0$ and $C = 0.006$. The fit of the equation to the impulse measured from the simulations in shown in Figure 3. A more detailed discussion of this impulse approximation is given in Appendix A.

We characterize the dissipative strength of a merger using the fractional impulse at the first pass, $f_k \equiv \Delta E / K_{\rm tot}$, where ΔE is the impulse and $K_{\rm tot}$ is the total initial internal kinetic energy of the galaxy, baryons and dark matter. We find that $f_{\rm new}$, the fraction of new stars formed in the merger relative to $M_{\rm tot}$, is indeed proportional to the fractional impulse and to the gas fraction $f_{\rm g}$,

$$f_{\rm new} = C_{\rm new}\ f_{\rm g}\ f_{\rm k}. \qquad (4)$$

The best fit to our simulations is obtained for $C_{\rm new} \sim 0.3$.

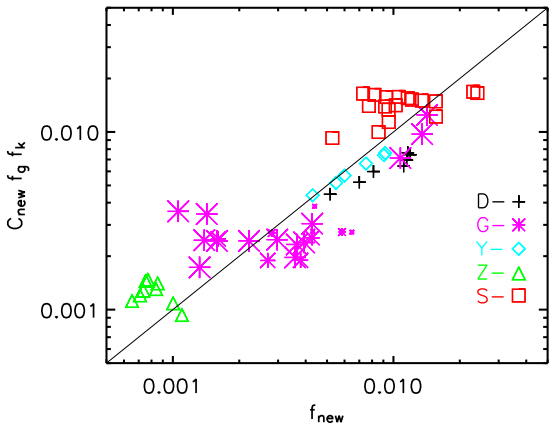

Figure 4. Fraction of new stars formed during the merger: the approximation based on gas fraction and impulse versus the actual value in the simulations. A stronger perturbation from a larger impulse enhances the collision rate between gas clouds, and thus induces more star formation.

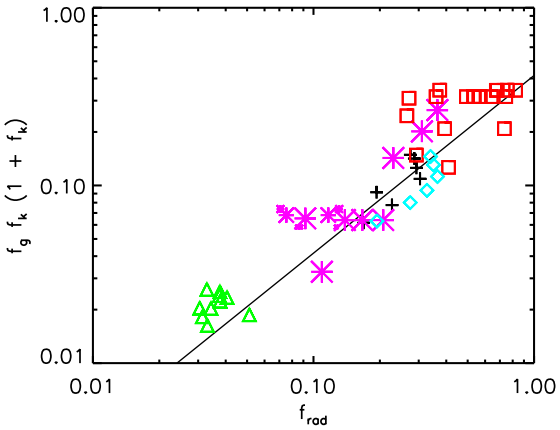

Figure 5. Fractional energy loss. The approximation of radiative losses in equation 6, which is based on gas fraction and impulse, is shown against the actual radiative energy losses. It demonstrates a crude proportionality, with the line plotted $y = 0.4x$.

The gas fraction determines the overall normalization of star formation, whereas the impulse factor tracks the variations with orbit. This prediction for the fraction of new stars is plotted in Figure 4 against the actual fraction of new stars in the simulated remnants. In order to consistently treat the star formation in simulations that were run for different lengths of time, and in keeping with previous work (Somerville et al. 2001), we separate star formation into a merger-induced burst component and a quiescent component. We accomplish this by subtracting out star formation measured from simulations of each progenitor in isolation. The quantity $f_{\rm new}$ in equation 4 refers to the burst component only.

Given the above correlation between impulse and star formation, we proceed to predict the energy loss by assuming that the colliding gas that forms new stars during the merger loses a constant fraction of its kinetic energy in the collision. In more detail, we make the following assumptions:

(i) Gas clouds have initial velocities approximately equal to the average initial velocities of the dark matter/baryon system.
(ii) The average impulse per mass imparted to gas that will form new stars is approximately equal to the average impulse per mass for the entire dark matter/baryon system.
(iii) The energy lost during the merger is proportional to the kinetic energy of the gas that will form stars. This includes: 1) the initial kinetic energy, and 2) the kinetic energy gained from the impulse.

While simplistic, these assumptions allow us to make a connection between radiative losses and star formation. Assumption (i) would be valid if the system resembled an isothermal sphere. Assumption (iii) provides a sensible way for parameterizing the energy loss, given that it is associated with collisions of gas clouds. Under this assumption, the radiative energy loss can be written as

$$E_{\rm rad} \propto (f_{\rm new}\ K_{\rm tot} + f_{\rm new}\ \Delta E). \quad (5)$$

The first term is the total initial internal kinetic energy of the gas that forms stars, and the second term is the energy imparted to that gas by the impulse. Dividing by K_{tot}, and using equation 4 gives

$$f_{\rm rad} \propto f_{\rm new}(1 + f_{\rm k}) \propto\ f_{\rm g}\ f_{\rm k}\ (1 + f_{\rm k}). \quad (6)$$

This expression is plotted in Figure 5 against the actual radiative energy losses in our simulations, showing a crude proportionality, with the proportionality constant ~ 0.4.

3.3 A Dissipative Model for Remnant Radii

Guided by this toy model for dissipative losses during a galaxy merger, we construct a modified energy conservation equation for predicting remnant radii. Note that the final stellar mass can be computed using the initial mass and the equation for star formation (4). We choose to include in our energy formula the initial stellar mass plus the mass of the stars formed during the merger, such that the dissipative term tracks the loss of energy of the progenitor's gas that becomes stars in the remnant. The energy equation is

$$E_{\rm int,f} = E_{\rm int,i} + E_{\rm rad} + E_{\rm orb}, \quad (7)$$

where the final and initial internal energies are

$$E_{\rm int,f} = -\frac{C_{\rm int} G (M_1 + M_2 + M_{\rm new,1} + M_{\rm new,2})^2}{R_{\rm f}} \quad (8)$$

$$E_{\rm int,i} = -C_{\rm int} G \left[\frac{(M_1 + M_{\rm new,1})^2}{R_1} + \frac{(M_2 + M_{\rm new,2})^2}{R_2} \right], \quad (9)$$

and M_1, M_2, R_1, and R_2 are the initial stellar masses and the corresponding three-dimensional half-mass radii of the progenitors, $R_{\rm f}$ is the final three-dimensional half-mass radius of the remnant, and $M_{\rm new,1}$ and $M_{\rm new,2}$ are the mass of new stars formed during the merger in galaxies one and two respectively, as predicted by our model. The constant structural parameter, which relates the internal energy of the systems to GM^2/R, is determined by best fit to the radii of

the simulated remnants to be $C_{\rm int} \simeq 0.5$. In assuming homology, we set the structural constants for the progenitors and remnants to the same value.

The radiated energy term is the sum of the losses from the two progenitors,

$$E_{\rm rad} = -C_{\rm rad}\Sigma_{i=1}^{2} K_i f_{{\rm g},i} f_{{\rm k},i}(1+f_{{\rm k},i}), \quad (10)$$

where K_i, $f_{{\rm g},i}$ and $f_{{\rm k},i}$ are the initial internal kinetic energy, gas fraction and impulse corresponding to progenitor i. The constant of proportionality relating our expression for energy loss to the actual energy lost is determined by best fit to the radii of the simulated remnants to be $C_{\rm rad} \simeq 1.0$.

The orbital energy is:

$$E_{orb} = -\frac{G(M_1+M_{\rm new,1})(M_2+M_{\rm new,2})}{R_{\rm sep}} + \frac{1}{2}(M_1+M_{\rm new,1})V_1^2 + \frac{1}{2}(M_2+M_{\rm new,2})V_2^2$$

where $R_{\rm sep}$, the distance between the progenitors' centres of mass, and V_1 and V_2, the centre of mass velocites of each progenitor, are defined at the beginning of the encounter. Most of our simulations are nearly parabolic, such that this term is close to zero.

Our model predictions for the remnant radii are plotted against the actual stellar half-mass radii of the simulated merger remnants in Figure 6. The overall scatter is $S = 0.21$, which is a significant improvement over the dissipationless model. There is no obvious systematic error, and the fit is good both for the wide range of progenitor properties and for the different choices of orbital parameters. The spread for a particular progenitor type results from differences in orbit and orientation. For most cases this orbital spread is well fit by the model. This is particularly evident with the D and Y series, for which only orbit is varied and not orientation. The spread in Sbc series is not quite as closely tracked by the model. This additional spread is the result of differing orientations. Orientation is not taken into account in the model for reasons described in §5.2. We note that the performance of the final model for radii is somewhat better than what might have been expected from the quality of the prediction of radiative losses, shown in 5. However, this is not as surprising if one remembers that radiative losses are only a correction on the non-dissipative model. Even if this correction is not exact, it always acts in the proper direction and makes the remnants more compact.

3.4 Velocity Dispersion

Naab et al. (2006) have shown that the kinematics of merger remnants change as a function of initial gas fraction. When predicting the central velocity dispersion of merger remnants we take gas fraction into account in two ways: first by using the gas fraction dependent predicted radius, and second by adjusting the central dark matter fraction to account for the rearrangement of gas and subsequent formation of new stars. In order to compute the stellar velocity dispersion of the merger remnants, we implement a virial relation of the type

$$\sigma^2 = C_{\rm vir}\frac{GM_{\rm dyn}}{R}, \quad (11)$$

where $M_{\rm dyn}$ is the dynamical mass of the system. This mass includes all of the stellar mass of the system and also a contribution from the dark matter near the centre of the galaxy. $C_{\rm vir}$ is a constant that varies slightly with galaxy structure and also accounts for the conversion between the three-dimensional radius and the projected, two-dimensional velocity dispersion. R is a characteristic radius (e.g., the stellar half-mass radius). σ is a line-of-sight velocity dispersion of stars inside the projected half-mass radius. We measure this from the simulations by averaging over 50 random projections.

Given the predicted values for $R_{\rm f}$ and the final stellar mass, one may attempt to estimate σ^2. However, variations in central progenitor dark matter fractions and differing amounts of star formation result in significantly different ratios of $M_{\rm dyn}$ to the total stellar mass in the remnants. Because we are dealing with an approximate virial relation of a system that actually is not completely self-gravitating, it is not obvious from first principles what the exact contribution to $M_{\rm dyn}$ from dark matter should be. We track the dark matter contribution by estimating the dark-matter fraction for each remnant. Therefore the uncertainty above, concerning which dark matter mass to include, translates into an uncertainty in which radius to choose for defining a dark-matter fraction. Because we use the three-dimensional stellar half-mass radius in our virial relation, it would be reasonable to choose a radius $\sim R_{\rm f}$. However, one can pick a range of radii and still achieve sensible results by making slight adjustments to $C_{\rm vir}$. We find the best results when we focus on the dark matter fraction inside *half* of the three-dimensional stellar half-mass radius. We define the dark-matter fraction within a given radius by

$$f_{\rm dm} = \frac{M_{\rm dm}}{(M_{\rm dm}+M_{\rm stars})}, \quad (12)$$

where $M_{\rm dm}$ and $M_{\rm stars}$ are the dark matter and stellar masses inside that radius, respectively. Much of the variation in the remnant dark matter fraction, $f_{\rm dm,f}$, is due to the variation in initial dark-matter concentrations and baryon distributions. However, another important effect is the tendency of new stars to form near the galaxy centre, causing mergers that form more stars to end up with lower $f_{\rm dm,f}$ values. We thus predict the final dark-matter fraction using the initial dark matter masses and our model prediction for the mass in new stars,

$$f_{\rm dm,f} = \frac{M_{\rm dm,1}+M_{\rm dm,2}}{M_{\rm dm,1}+M_{\rm dm,2}+C_{\rm stars}(M_1+M_2+M_{\rm new})}. \quad (13)$$

$M_{\rm dm,1}$ and $M_{\rm dm,2}$ are the dark matter masses inside half of the three-dimensional stellar half-mass radii of the progenitors. M_1 and M_2 are the stellar masses of the progenitors, and $M_{\rm new}$ is the total mass of stars formed during the merger as predicted by equation 4. This expression simply assumes that the inner region of the remnant contains the same amount of dark matter as the sum of the inner regions of the progenitors, and that a fixed fraction, $C_{\rm stars}$, of the final stellar mass is inside one-half of the three-dimensional stellar half-mass radius. We find that the best fit to the simulated remnants is $C_{\rm stars} \simeq 0.35$.

Our modified virial relation becomes

$$\sigma^2 = C_{\rm vir}\frac{G(M_1+M_2+M_{\rm new})}{R_{\rm f}(1-f_{\rm dm,f})}. \quad (14)$$

The best-fitting value from our simulations is $C_{\rm vir} \simeq 0.30$. The model predictions for the stellar line-of-sight velocity

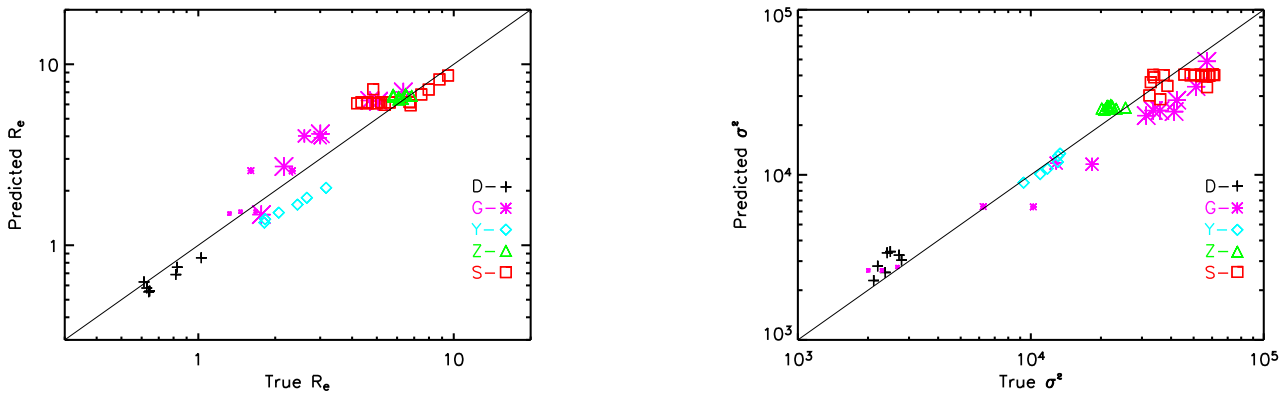

(a) (b)

Figure 6. The model predictions for radius (a) and velocity dispersion (b) versus the actual values. Predicted R_e and True R_e are the predicted and simulated values of the three-dimensional stellar half-mass radius of the remnants, respectively. σ is the line-of-sight velocity dispersion inside the projected half-mass radius. The scatter is $S = 0.21$ for the radius prediction and $S = 0.24$ for σ^2.

dispersions are shown in Figure 6, in comparison with the simulated values. The scatter in σ^2 is $S = 0.24$, and the overall performance is similar to that of the model for the final radii. There are no obvious systematic errors, and the predictions properly capture the variations due to either progenitor properties or orbital parameters.

4 UNEQUAL MASS MERGERS

The cases studied so far were mergers of identical galaxies, and the model was built using the simulations of these cases. However, most mergers in the universe are of unequal mass galaxies. More recent simulations were run of unequal mass mergers (Cox et al. 2007), and given the importance of unequal mass mergers in the real universe we here examine the accuracy of our model for different progenitor mass ratios. For this study we used simulations of unequal mass mergers from the G series of galaxies (Cox et al. 2007). These mergers cover a range of mass ratios and a variety of orbital parameters. For unequal mass mergers, the predictions of remnant properties remain relatively accurate with $S = 0.13$ about the previously fit relation for radii, and $S = 0.20$ for σ^2 (see Figure 7). Note that in some cases the spread does not fall directly along the line. This is the result of a number of simulations with the same progenitors and orbital parameters, but with different orientations of the progenitors with respect to the orbital plane. Variations due to orientation do not have clear enough systematics to be accounted for in the model. We discuss this limitation in §5.2.

In major mergers, which have mass ratios greater than 1:3, the gas disks of the galaxies are severely disrupted, and we see large flows of gas toward the galactic centres. However, in minor mergers, which have mass ratios less than 1:3, these flows are much less pronounced because the gas disk of the larger progenitor is only modestly disrupted. For example, central gas densities in a major merger of two G3 galaxies reach values roughly four times that of a minor merger (1:6) of G3 and G1 galaxies on the same orbit. Hence, dissipation is expected to be much less important in the centres of the big progenitors of minor mergers. Our model captures this effect through the impulse dependence of the radiation term. For minor mergers where $M_{\rm big} \gg M_{\rm small}$, the radiation term becomes insignificant in comparison to the internal energy term. It is also worth noting that the the star formation equation (4) under predicts star formation in the smaller progenitor in this extreme minor merger regime. However, this has little effect on the predictions of remnant properties since the mass of new stars formed in a much smaller progenitor is much smaller than the mass of the larger progenitor.

5 CAVEATS

5.1 Feedback

Arguably the largest uncertainty in the physics of our simulations is in the prescription for feedback. The merger simulations fit by our model all use the same prescription for feedback with the same parameters, hence, it would be useful to vary these feedback parameters and examine the effect on our model. The feedback recipe is characterized by two parameters: feedback efficiency and an equation of state parameter, n, which sets the polytropic index. The effective pressure is

$$P_{eff} \sim \rho^{1+(n/2)}. \quad (15)$$

We explore three equations of state, $n = 0$, $n = 1$, and $n = 2$, where $n = 0$ corresponds to an isothermal equation of state and $n = 2$ results in a stiff equation of state. The feedback efficiency determines how quickly the feedback energy is allowed to thermalize. Higher efficiencies result in a quicker dissipation of the feedback energy. For each value of n, we examine two different values of efficiency. As a lower limit, we use a low efficiency value that gives just enough pressure to stabilize the disk. We also simulate cases of super-stable disks where the efficiency is set to ten times that needed for disk stabilization. In table 2, labels of the feedback parameter sets denote the values of n

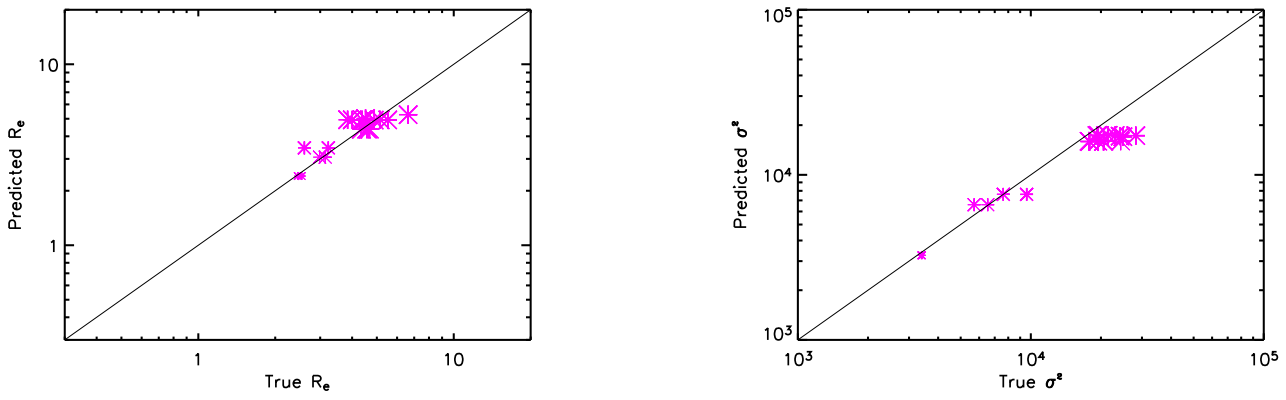

Figure 7. Unequal Mass Mergers. The predicted values of our radius and velocity dispersion models versus the actual values for unequal mass mergers of G series galaxies. $S = 0.13$ for radius, and $S = 0.20$ for σ^2.

Table 3. Effect of differing feedback parameters on remnant properties. All simulations in the table are variations of a fiducial Sbc merger. $M_{\rm newstars}$ is the total mass in new stars formed during the 3 Gyr simulation, burst and quiescent. $R_{\rm f,1/2}$ is the stellar *three-dimensional half-mass radius* of the remnant. $\sigma_{\rm f}$ is the velocity dispersion of the remnants measured inside of the *projected half-mass radius* averaged over 50 random projections.

Model	$M_{\rm newstars}$ ($10^{10}{\rm M}_\odot$)	$R_{\rm f,1/2}$ (kpc)	$\sigma_{\rm f}$ (km s^{-1})
n0med	5.75	5.37	253
n0high	2.68	5.72	218
n1med	5.30	5.34	252
n1high	2.57	5.75	190
n2med(fiducial)	5.03	5.62	225
n2high	1.61	6.95	178

and efficiency chosen. Unstable cases with even lower feedback efficiency were run but are not discussed here. Thus, for consistency our "low" efficiency cases are labeled "med"(e.g. *n2med* means $n = 2$ and the feedback efficiency is low). In general, with lower feedback, the maximum star formation rate is higher, but the starburst duration is shorter. For a more detailed description of our feedback model see Cox et al. (2006, 2007).

To examine the effects of feedback on our remnant model, we take the fiducial Sbc merger and simulate identical initial conditions with varied values of the feedback parameters. As expected, feedback has a significant effect on star formation. The effect is twofold. First, both increased feedback efficiency and, to a smaller extent, stiffer equations of state (higher n) decrease the total number of stars formed. This can be a dramatic effect. As shown in Table 3 the total number of stars formed varies by more than a factor of three. Secondly, feedback can change the radial distribution of stars formed. A stiffer equation of state will lead to more stars being formed at large radii (Cox et al. 2006).

Both of these effects can act in concert to increase the size of the merger remnant. However, the effect is weak enough that it takes both high feedback efficiency and a stiff equation of state to significantly alter the final half-mass radius (see Figure 8). In our set of feedback models, the only model for which the radius is significantly different than the others is *n2high*. Even in this model the remnant radius is only a factor of ~ 1.3 larger than the most compact remnant. Differences in radius and compactness will also affect the central velocity dispersion. Higher efficiency and stiffer feedback models produce somewhat lower σ. This effect is similar in magnitude to the effect on radius, with a factor of ~ 1.4 between the largest and smallest σ. For velocity dispersion, our fiducial model lies near the centre of the distribution (see Figure 8). These differences are roughly comparable to the scatter in our remnant model.

While we have chosen a specific feedback model as a fiducial, and used it to run most of our cases, we note that there are currently no theoretical or observational motivations for this choice. Feedback in the real universe could resemble any of these models. If feedback in the real universe is significantly different from our fiducial case, then it is possible that the parameters of our model would require some tuning. $C_{\rm new}$ is the parameter most affected by differing feedback. The variations in star formation suggest that $C_{\rm new}$ could vary roughly from 0.1 to 0.35. It is also possible that the structural parameters $C_{\rm int}$, $C_{\rm vir}$, and $C_{\rm stars}$ would need to be adjusted. However, aside from the mass of new stars, the relatively drastic changes in feedback produce relatively minor changes in remnant properties. This suggests that any tuning needed to match the real universe would be small. Further verification of the model will require testing with independent feedback recipes.

5.2 Orbits

There are several potential sources of uncertainty concerning our treatment of the initial orbits of the progenitors. The first regards the orbital energy term in our energy conservation equation. Cole et al. (2000) assume in their dissipationless model that some of the orbital energy is transferred

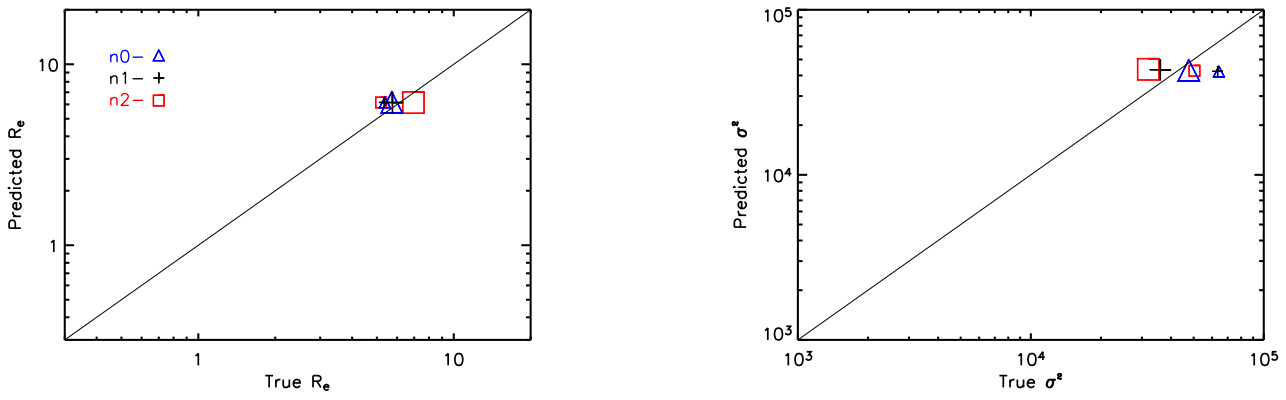

(a) (b)

Figure 8. Various feedback models. The predicted values of radius (a) and velocity dispersion (b) for all of the variations on the feedback model. Large symbols represent high feedback efficiency, small symbols represent low efficiency, and squares, crosses, and triangles represent n=2, n=1, and n=0 respectively.

to the outer dark matter halo through dynamical friction. In order to estimate the energy transferred from the orbit to the baryonic remnant, they assume that the two galaxies come into a circular orbit at a radius that equals the sum of their half-mass radii. However, the orbits in our simulations actually tend to quickly radialize after the first close passage. We therefore adopt the better approximation that all the orbital energy ends up in the baryonic remnant. This too may be an over-simplification, as the energy deposited in the dark halo is likely to depend on the initial eccentricity of the orbit, and may get larger for increasingly tangential orbits. Unfortunately, our suite of simulations is not particularly well-suited to exploring this dependence, as most of them start with initial orbital eccentricities close to unity. Our suite does contain three Sbc simulations and one Z simulation with $e = 0.8$, and also one unequal mass merger, a G3-G2, with an initially circular orbit, $e = 0$. We find that these few cases are well fit by our model as is. However, given our limited sampling of non-radial orbits, we keep in mind that our orbital-energy term may require some modification. On the other hand, we note that statistical studies of cosmological merger orbits suggest that they tend to be rather radial (Benson 2005; Khochfar & Burkert 2006), and that all attempts we made to include a term for energy transfer to the dark matter did not significantly improve the model.

A second potential concern is the initial orbital parameters we use. Our simulations typically start when the centre of one galaxy is near half of the virial radius of the other galaxy, whereas the typical analysis of halo orbits in N-body simulations refer to orbits at the virial radius (Benson 2005; Khochfar & Burkert 2006). Furthermore, our simulations involve the final entry into this radius, whereas in cosmological situations many of the halos enter and leave the virial radius more than once before merging. One practical concern is how to convert between orbits at $0.5\,R_{\rm vir}$ and at $R_{\rm vir}$. Dynamical friction undoubtedly induces some evolution in the orbital parameters as the galaxies fall between $0.5\,R_{\rm vir}$ and $R_{\rm vir}$. This effect should be evaluated using cosmological N-body simulations.

Finally, our model does not take into account the effect of the initial orientation of the progenitors with respect to the orbital plane. Our suite of simulations does include a number of different initial orientations, including both prograde and retrograde encounters. Previous authors have observed systematic differences between encounters with different orientations (Naab et al. 2006; Barnes 2002), but the effects on the remnants in our simulations do not show clear enough systematics for us to effectively characterize them. The performance of the model could be improved by including a term that depends on orientation, but the modest improvement did not seem to justify the inclusion of yet another parameter that would increase both the complexity of the model and the risk that the model is over-fit.

5.3 Gas Fraction

Our merger suite primarily consists of disky progenitors with high gas fractions. It is possible that we are missing some of the effects that dominate the results of dry mergers of spheroids. For example, Boylan-Kolchin et al. (2006) find that more radial encounters of dry ellipticals result in larger remnants. However, we see no evidence for such a trend, not even in our lowest gas fraction simulations, the Z series, where $M_{gas}/M_{baryon} = 0.1$. In fact, for these low-gas cases, we see essentially no systematic trend of remnant size with orbit, and a generally smaller scatter in remnant size. We conclude that if we miss any effect of this sort, it is likely to be small. Apparently, the dissipationless energy conservation equation becomes a relatively accurate approximation in the limit of low gas fraction, and our model converges to the dissipationless model when the progenitors are gas-free.

Another limitation of our model is that it is unlikely to apply to extremely gas-rich mergers, where $M_{\rm gas} \gg M_{stars}$. For such cases the initial energy term should account for the size of the gas disk, whereas our model only takes into account the initial size of the stellar disks. The highest gas fraction case that we include has a ratio of $M_{\rm gas}/M_{\rm stars} = 3.1$. For the cases that we simulate, where $M_{\rm gas} \lesssim M_{\rm stars}$ we find that the final sizes are relatively insensitive to the initial sizes of the gas disks. Specifically, our suite includes

cases where the gas disk scale length is equal to the stellar disk scale length and cases where the gas disk scale length is three times the stellar disk scale length. Both of these cases are well fit by our model.

One final note is that our merger simulation suite does not attempt to model galaxies at higher redshift by systematically changing gas fraction and concentration as has been done in other studies (Robertson et al. 2006). Since progenitors are primarily modeled after low-redshift galaxies, this is the regime where the model is calibrated best. However, the model is based on simple physical principles and is robust to systematic changes in gas and bulge fraction.

6 CONCLUSIONS

We have developed a simple toy model for the physical processes involved in wet mergers of galaxies, and have calibrated it using a suite of hydrodynamical merger simulations. This modeling helped us to gain a better understanding of these processes, and provides a practical semi-analytic recipe for predicting post-merger galaxy properties in SAMs.

Crude models of this sort have been used by Cole et al. (2000), Hatton et al. (2003), and Shen et al. (2003), but these models did not account for energy losses through dissipative processes, and they have not been calibrated against realistic merger simulations. Using a suite of merger simulations, we have demonstrated the key role of dissipative energy losses in determining the final radii and velocity dispersions of merger remnants. We found that the dissipative effects depend on the initial orbits of the progenitors. More violent, lower angular momentum orbits create greater disturbances in the gas disks, which in turn radiate more energy and produce more stars. This orbital "violence" can be parameterized through an impulse approximation for energy exchange between the orbital and internal components during the first close pass of the encounter.

We present a physically-motivated, simulation-calibrated model that is capable of predicting star formation, central dark matter fraction, remnant radius and remnant velocity dispersion, given the properties of the progenitors and the initial orbital parameters of a merger.

The non-dissipative energy conservation model often predicts radii that are off by a factor of $\sim 2-3$, and it does not reproduce the spread due to orbital variations. Our model, which accounts for the dissipative energy losses, results in only $\sim 25\%$ errors in the predicted radius and velocity dispersion when a wide variety of progenitor types is considered. For a given progenitor type, the error in remnant properties is reduced to $\sim 10\%$, indicating that our model correctly captures the variation of remnant properties due to merger orbit.

Since we used the whole available simulation suite to calibrate our model, via a few proportionality constants of order unity, a proper evaluation of the model performance is yet to be pursued using an independent suite of simulations.

7 ACKNOWLEDGMENTS

We thank Greg Novak and Simon White for helpful discussions. This material is based upon work supported under a National Science Foundation Graduate Research Fellowship granted to MC. The research of MC was also supported by a University of California/Lawrence Livermore National Laboratory cooperative grant from the Institute of Geophysics and Planetary Physics to Wil van Breugel. Research of MC, AD, and JRP was supported by NSF AST-0205944 and NASA NNX07AG94G. Research of AD was also supported by ISF 213/02, by GIF I-895-207.7/2005, by the Einstein Center at HU, and by NASA ATP NAG5-8218. Research of PJ was supported by HST-AR-10678 and 10958, provided by NASA through grants from the Space Telescope Science Institute, which is operated by the Association of Universities for Research in Astronomy, Incorporated, under NASA contract NAS5-26555. This research used the Beowulf UpsAnd at UCSC and computational resources of the National Energy Research Scientific Computing Center, which is supported by the Office of Science of the U.S. Department of Energy under Contract No. DE-AC02-05CH11231.

REFERENCES

Aguilar L. A., White S. D. M., 1985, ApJ, 295, 374
Barnes J. E., 2002, MNRAS, 333, 481
Benson A. J., 2005, MNRAS, 358, 551
Binney J., Tremaine S., 1987, Galactic dynamics. Princeton, NJ, Princeton University Press, 1987, p.747
Blumenthal G. R., Faber S. M., Primack J. R., Rees M. J., 1984, Nature, 311, 517
Boylan-Kolchin M., Ma C.-P., Quataert E., 2006, MNRAS, 369, 1081
Ciotti L., Lanzoni B., Volonteri M., 2007, ApJ, 658, 65
Cole S., Lacey C. G., Baugh C. M., Frenk C. S., 2000, MNRAS, 319, 168
Cox T. J., 2004, PhD thesis, UC Santa Cruz
Cox T. J., Jonsson P., Primack J. R., Somerville R. S., 2006, MNRAS, 373, 1013
Cox T. J., Jonsson P., Somerville R. S., Primack J. R., A. D., 2007, in prep
Dekel A., Cox T. J., 2006, MNRAS, 370, 1445
Dekel A., Shaham J., Lecar M., 1980, ApJ, 241, 946
Hatton S., Devriendt J. E. G., Ninin S., Bouchet F. R., Guiderdoni B., Vibert D., 2003, MNRAS, 343, 75
Jonsson P., 2006, MNRAS, 372, 2
Jonsson P., Cox T. J., Primack J. R., Somerville R. S., 2006, ApJ, 637, 255
Kennicutt R. C., 1998, ApJ, 498, 541
Khochfar S., Burkert A., 2006, A&A, 445, 403
Mihos J. C., Hernquist L., 1994, ApJL, 437, L47
Mo H. J., Mao S., White S. D. M., 1998, MNRAS, 295, 319
Naab T., Jesseit R., Burkert A., 2006, MNRAS, 372, 839
Naab T., Khochfar S., Burkert A., 2006, ApJL, 636, L81
Richstone D. O., 1975, ApJ, 200, 535
Robertson B., Cox T. J., Hernquist L., Franx M., Hopkins P. F., Martini P., Springel V., 2006, ApJ, 641, 21
Shen S., Mo H. J., White S. D. M., Blanton M. R., Kauffmann G., Voges W., Brinkmann J., Csabai I., 2003, MNRAS, 343, 978
Somerville R. S., Primack J. R., Faber S. M., 2001, MNRAS, 320, 504
Springel V., Hernquist L., 2002, MNRAS, 333, 649

Springel V., Yoshida N., White S. D. M., 2001, New Astronomy, 6, 79
Toomre A., 1977, in Evolution of Galaxies and Stellar Populations Mergers and Some Consequences. p. 401
Toomre A., Toomre J., 1972, ApJ, 178, 623

8 APPENDIX A: IMPULSE APPROXIMATION

A number of previous researchers have studied and parameterized the transfer of orbital to internal kinetic energy during galaxy encounters (Richstone 1975; Dekel et al. 1980; Aguilar & White 1985). Binney & Tremaine (1987) summarize these studies and present formulas for impulse approximations valid in the tidal and radial cases. Aguilar & White (1985) find that the tidal approximation breaks down at approximately $5R_e$, but that a smooth interpolation between the two cases gives an approximate fit to actual energy transfers:

$$Tidal\ case: \qquad \Delta E = \frac{2G^2 M_1 M_2^2 \bar{r^2}}{3R_{\rm peri}^4 V_{\rm peri}^2} \tag{16}$$

$$Radial\ case: \qquad \Delta E = \frac{3G^2 M_1 M_2^2}{3V_{\rm peri}^2 a^2} \tag{17}$$

M_1 and M_2 are the masses of the perturbed and perturbing galaxies respectively, and $R_{\rm peri}$ and $V_{\rm peri}$ are the pericentric distance and velocity. For the tidal case, $\bar{r^2}$ is the mean-square radius of the perturbed galaxy. A Plummer model, $\Phi = -GM/\sqrt{r^2+a^2}$, is assumed for the radial approximation.

We measure the change in internal kinetic energy of each progenitor during the first close encounter and define this as our "impulse." In order to compare with the above approximations we assume that the galaxies are point masses and use values of $R_{\rm peri}$ and $V_{\rm peri}$ calculated at the beginning of the simulations. The impact parameters simulated in our suite all fall well within $5R_{\rm dm}$, as might be expected for *merger* orbits. Consequently, the tidal approximation performs quite poorly at predicting the impulse. Furthermore, any impulse approximation assumes that the dynamical time of the perturbed galaxy is much less than the time of the encounter. However, if two galaxies are going to merge, then the encounter velocity is typically of the same order as the internal velocity of the larger galaxy. Therefore, it is not clear that either impulse approximation above would apply. We compared the radial approximation, and several similar functions that included a dependence on impact parameter, to the measured impulses and found that they did not provide satisfactory fits.

However, we do find that the measured impulse, during an encounter with orbital parameters within our range of simulated values, is well-fit by the following formula:

$$\Delta E = \frac{AG^2 M_{1,\rm tot}^2 M_{2,\rm tot}}{V_{\rm peri}^2 (R_{\rm peri}^2 + B\ R_{1,\rm tot}\ R_{\rm peri} + C\ R_{1,\rm tot}^2)}, \tag{18}$$

where $M_{1,\rm tot}$ and $M_{2,\rm tot}$ are the total mass of the perturbed and perturbing galaxies respectively, baryons plus dark matter, and $R_{1,\rm tot}$ is the total half mass radius of the perturbed galaxy. The parameters are set by best fit to the simulation results with $A = 1.6$, $B = 1.0$, and $C = 0.006$.

For a radial orbit, this formula vaguely resembles the radial approximation. However, the mass dependence of the formula is different. In the radial impulse approximation $\Delta E \propto M_1 M_2^2$, whereas in our formula $\Delta E \propto M_1^2 M_2$. This suggests that the impulse approximation is breaking down, that we cannot simply assume that the potential of the perturbed galaxy is constant during the encounter. At intermediate impact parameters, where $R_{\rm peri} < R_{1,\rm tot}$, the fitting formula falls off as $1/R_{\rm peri}$. At larger impact parameters, $R_{peri} > R_{dm}$, it falls off as $1/R_{peri}^2$. The parameter C sets the cutoff radius at which the impulse ceases to increase with decreasing impact parameter and approaches the constant radial case. The fit of C is somewhat tenuous since our simulations do not actually probe the range of $R_{peri}^2 < CR_{dm}^2$. However, these cases are so radial that the probability of such encounters is low, and the effects of small changes in C are likely to be insignificant. Our suite probes a range of roughly $0.1R_{1,\rm tot} < R_{\rm peri} < 2R_{1,\rm tot}$ and $2\sigma_{\rm prog} < V_{\rm peri} < 10\sigma_{\rm prog}$, where $\sigma_{\rm prog}$ is the initial velocity dispersion of the larger progenitor. The formula is plotted against impulses measured from our simulations in Figure 3. This plot includes both equal and unequal mass mergers. The fit is valid over a range of progenitor mass distributions. Specifically, the structure of the fitted galaxies varies widely with a variety of bulge fractions and dark matter concentrations.

9 APPENDIX B: SUMMARY OF THE MODEL

The model presented requires the integration of formulas and ideas found throughout the paper. Hence, for pragmatic purposes, we present a brief summary of the model for the reader who wishes to implement it as a recipe within a semi-analytic model of galaxy formation. In Figure 9 we illustrate the outline of the model. The relevant equations are included, except for the definitions of the energy terms in the conservation equation. For these, we refer the reader to the list in §3.3. Inputs, parameters, and outputs are defined in Tables 4, 5, and 6.

The general flow of the model is as follows:

1. Use orbits and masses to calculate impulse.
2. Use impulse and gas fraction to calculate new stars formed in the burst.
3. Use mass of new stars and properties of progenitors to calculate radius.
4. Use initial dark matter fraction and final mass of stars to calculate remnant central dark matter fraction.
5. Use central dark matter fraction and radius to calculate velocity dispersion.

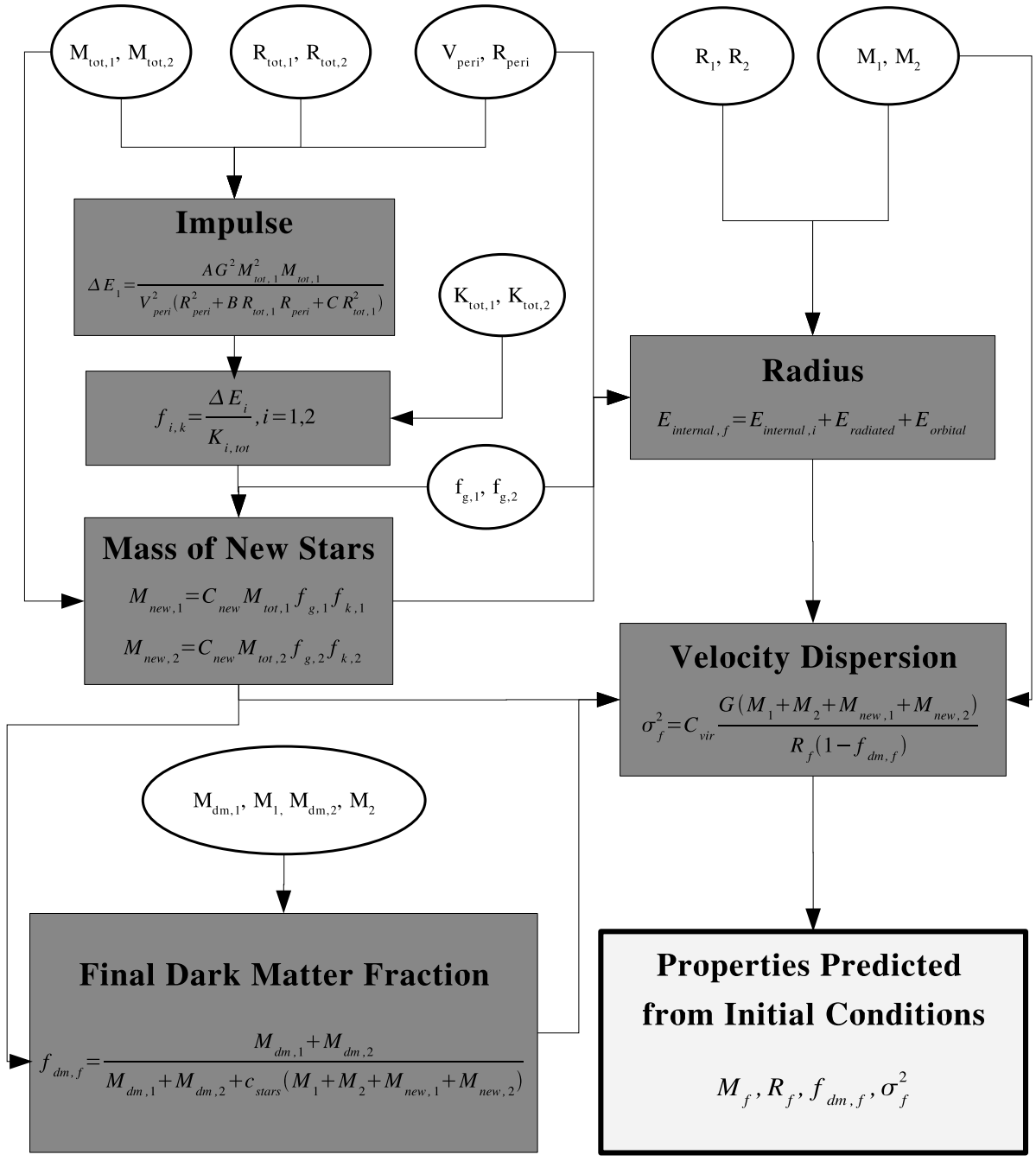

Figure 9. Summary of the inputs (ovals), outputs (white rectangle), and equations (shaded rectangles) needed to implement the merger model.

Table 4. Definitions of the inputs used in the model.

Name	Definition
Inputs	
$M_{\rm tot,1}, M_{\rm tot,2}$	The total masses (baryonic plus dark) of galaxies 1 and 2 respectively.
$R_{\rm tot,1}, R_{\rm tot,2}$	The three-dimensional half-mass radii of the total masses (baryonic plus dark) of galaxies 1 and 2 respectively.
$V_{\rm peri}, R_{\rm peri}$	The theoretical pericentric velocity and distance of the first encounter, defined when the galaxies are separated by $\sim R_{vir}$.
$K_{\rm tot,1}, K_{\rm tot,2}$	The total kinetic energies of the galaxy/halo systems of galaxy 1 and 2 respectively. In our simulations $K_{\rm tot,1} \simeq 0.35\ GM^2_{\rm tot,1}/R_{\rm tot,1}$ with very little scatter.
$f_{\rm g,1}, f_{\rm g,2}$	The gas fractions of galaxies 1 and 2, defined as (gas mass)/(total mass).
R_1, R_2	The stellar three-dimensional half-mass radii of galaxies 1 and 2.
M_1, M_2	The stellar masses of galaxies 1 and 2.
$M_{\rm dm,1}, M_{\rm dm,2}$	The dark matter mass inside 1/2 the stellar three-dimensional half-mass radius of galaxies 1 and 2 respectively.
$M_{\rm stars,1}, M_{\rm stars,2}$	The stellar mass inside 1/2 the stellar three-dimensional half-mass radius of galaxies 1 and 2 respectively.

Table 5. Definitions of the parameters used in the model.

Name/Value	Description
Parameters	
$A = 1.6$ $B = 1.0$ $C = 0.006$	Parameters fit to match the impulse model to the simulations. See Appendix A.
$C_{\rm new} = 0.3$	Proportionality constant in star formation equation. Determines mass of new stars.
$C_{\rm int} = 0.5$	Structural constant which sets relative weighting of internal energy.
$C_{\rm rad} = 1.0$	Constant which sets relative weighting of radiated energy.
$C_{\rm sig} = 0.30$	Structural constant which sets proportionality of σ^2 to M/R in remnants.
$C_{\rm stars} = 0.35$	Sets fraction of stars within 1/2 of the half-mass radius of the remnants.

Table 6. Definitions of the outputs used in the model.

Name	Definition
Outputs	
$M_{\rm f}$	Mass of stars in the remnant (old + burst).
$R_{\rm f}$	Stellar three-dimensional half-mass radius of remnant.
$f_{\rm dm,f}$	The dark matter fraction inside 1/2 of $R_{\rm f}$
$\sigma_{\rm f}$	The stellar velocity dispersion of the remnant inside the projected half-mass radius.